

# A Hardware-Efficient Photonic Tensor Core: Accelerating Deep Neural Networks with Structured Compression

Shupeng Ning,<sup>a</sup> Hanqing Zhu,<sup>a</sup> Chenghao Feng,<sup>a</sup> Jiaqi Gu,<sup>b</sup> David Z. Pan,<sup>a</sup> and Ray T. Chen<sup>a,\*</sup>

<sup>a</sup> *Department of Electrical and Computer Engineering, The University of Texas at Austin,  
Austin, Texas 78758, United States*

<sup>b</sup> *School of Electrical, Computer and Energy Engineering, Arizona State University,  
Tempe, Arizona 85281, United States*

\**Email: [chenrt@austin.utexas.edu](mailto:chenrt@austin.utexas.edu)*

## Abstract

Recent advancements in artificial intelligence (AI) and deep neural networks (DNNs) have revolutionized numerous fields, enabling complex tasks by extracting intricate features from large datasets. However, the exponential growth in computational demands has outstripped the capabilities of traditional electrical hardware accelerators. Optical computing offers a promising alternative due to its inherent advantages of parallelism, high computational speed, and low power consumption. Yet, current photonic integrated circuits (PICs) designed for general matrix multiplication (GEMM) are constrained by large footprints, high costs of electro-optical (E-O) interfaces, and high control complexity, limiting their scalability. To overcome these challenges, we introduce a block-circulant photonic tensor core (CirPTC) for a structure-compressed optical neural network (StrC-ONN) architecture. By applying a structured compression strategy to weight matrices, StrC-ONN significantly reduces model parameters and hardware requirements while preserving the universal representability of networks and maintaining comparable expressivity. Additionally, we propose a hardware-aware training framework to compensate for on-chip nonidealities to improve model robustness and accuracy. We experimentally demonstrate image processing and classification tasks, achieving up to a 74.91% reduction in trainable parameters while maintaining competitive accuracies. Performance analysis expects a computational density of 5.84 tera operations per second (TOPS) per mm<sup>2</sup> and a power efficiency of 47.94 TOPS/W, marking a 6.87× improvement achieved through the hardware-software co-design approach. By reducing both hardware requirements and control complexity across multiple dimensions, this work explores a new pathway to push the limits of optical computing in the pursuit of high efficiency and scalability.

**Keywords:** optical neural network, artificial intelligence, photonic integrated circuits, compression, optical computing, hardware efficiency

## Introduction

Machine learning (ML) with DNNs has transformed various aspects of science and technology,<sup>[1]</sup> including object recognition,<sup>[2]-[4]</sup> autonomous driving,<sup>[5]</sup> natural language processing,<sup>[6][7]</sup> and medical diagnosis.<sup>[8][9]</sup> Additionally, the emergence of large language models (LLMs) has further demonstrated human-level intelligence in specific tasks.<sup>[10][11]</sup> The unprecedented advancements of modern DNNs are driven by rapidly expanding model sizes—with millions to tens of billions of parameters—and increasing data volumes, which allow for the extraction of intricate, high-level features needed for complex tasks.<sup>[1][11][12]</sup> Notably, these improvements in model performance have led to a surge in demand for computing resources and memory access. DNNs typically comprise multiple cascaded layers, where data are represented as vectors processed through matrix-vector multiplications (MVMs) with corresponding weights, which are the main contributors to time and energy consumption. To efficiently execute MVMs, hardware AI accelerators—including, but not limited to, graphical processing units (GPUs), field-programmable gate arrays (FPGAs),<sup>[13][14]</sup> and application-specific integrated circuits (ASICs)<sup>[15]</sup>—have been widely developed by both industry and academia. However, as integrated circuits scale to include tens of billions of transistors operating at gigahertz (GHz), they encounter saturated energy efficiency, heat dissipation issues, and limited bandwidth, making electrical processors unsustainable for meeting surging demands.<sup>[16]</sup> Moreover, as semiconductor processes advance to sub-nanometer nodes and approach the inherent physical limitations of devices, the unreliability caused by quantum uncertainties has become another bottleneck for further scaling.<sup>[16][17]</sup> Pursuing higher computing density, power efficiency, and scalability remains a persistent goal in developing high-performance AI accelerators.<sup>[18]</sup>

Due to the aforementioned intrinsic bottlenecks, the exploration of novel technologies beyond traditional electrical digital computing has emerged as an attractive trend.<sup>[20]-[24]</sup> Among these, optical neural networks (ONNs) based on PICs are promising candidates for AI accelerators. The inherent high computational speeds, low power consumption, low latency, and high parallelism enabled by the unique multiplexing techniques of optical computing can effectively overcome the aforementioned issues.<sup>[25]</sup> Additionally, advances in silicon photonics allow for the implementation of optical computing on low-cost PICs with high integration density using CMOS-compatible fabrication processes. Over the past decade, various PIC-based ONN prototypes have been presented, demonstrating the implementation of multilayer perceptrons (MLPs),<sup>[22][23]</sup> convolutional neural networks (CNNs),<sup>[24][26][27]</sup> spike neural networks (SNNs),<sup>[28]</sup> *etc.* However, a primary challenge in contemporary PICs arises from the micron- to millimeter-scale dimensions of on-chip photonic devices, which leads to unavoidable trade-offs between the PIC scaling and the chip footprint.<sup>[25]</sup> Furthermore, the peripheral electrical components for E-O modulation, data

access, and conversion between analog and digital domains boost energy consumption, thereby undermining the power efficiency benefits of optical computing.

To address these challenges associated with implementing large-scale MVMs on PICs,<sup>[26]</sup> it is necessary to explore strategies that extend beyond device- or circuit-level innovations. One critical strategy is domain-specific hardware customization informed by algorithm-level insights, which can significantly improve the efficiency and scalability of photonic tensor cores (PTCs). Recent research indicates that DNNs, especially CNNs, are often over-parameterized with significant redundancy in their parameters.<sup>[19][29]</sup> This redundancy leads to unnecessary power consumption, prolonged runtimes, and increased memory usage, which has driven extensive research into algorithm-level model compression techniques such as connection pruning,<sup>[30][31]</sup> low-rank approximations,<sup>[32][33]</sup> and structured model designs.<sup>[19][34]</sup> These approaches have demonstrated substantial improvements in hardware efficiency with minimal performance trade-offs, making them highly relevant for optimizing optical computing systems. In our prior research,<sup>[35][36]</sup> we proposed the butterfly-style PTC and were the first to apply model compression techniques on the PIC platform. However, the mesh configuration of this architecture results in a large footprint. Moreover, the phase tuning mechanism presents significant challenges for calibration and precise programming. These factors collectively restrict its ability to fully leverage the efficiency benefits that novel algorithms might offer.

In this work, we advance the exploration of model compression techniques for optical computing by introducing a customized StrC-ONN architecture with the CirPTC. On the algorithmic side, StrC-ONN represents weight matrices using block-circulant matrices (BCMs) with restricted parameter spaces, effectively eliminating redundant parameters and unlocking the potential for designing customized ONN structures to fully harness their efficiency. From the hardware perspective, a compact microring resonator (MRR) crossbar array is specifically designed to implement BCMs, thereby minimizing E-O interface costs while achieving superior area and energy efficiency. Unlike the butterfly-style PTC, CirPTC directly imposes a structured compression through its circuit topology, thereby eliminating the need for complex calibration. Moreover, the cascading between each building block simplifies the control of modulation deviations compared to mesh-based PICs. To address on-chip nonidealities, we propose and experimentally deploy a hardware-aware training framework that compensates for these imperfections, enhancing model performance and robustness. We experimentally demonstrate the image processing capabilities of our design using convolutional kernels on CirPTC. Furthermore, we evaluate the end-to-end accuracy of StrC-ONN on various image classification tasks, including the SVHN, CIFAR-10, and COVID-QU-Ex datasets. This approach achieves up to a 74.91 % reduction in trainable parameters, active modulators and memory requirements, while maintaining

comparable accuracy to conventional GEMM-based digital DNNs. Performance analysis reveals that the design can achieve a computational density of 5.84 TOPS/mm<sup>2</sup>, with a power efficiency of 47.94 TOPS/W—representing a 6.87× improvement enabled by the dedicated hardware-software co-design strategy—after appropriate scaling and a unique spectral folding technique. Therefore, the proposed architecture and CirPTC offer a promising solution to fully harness the potential of optical computing, paving the way for next-generation AI hardware with enhanced performance and power efficiency.

## Concept and Principle

### ONN with Structured Compression

The structured compression, compared to other compression techniques, reduces both computational complexity and storage complexity while maintaining a regular network connection topology. An  $M \times N$  BCM, for instance, is composed of  $P \times Q$  blocks, each order- $l$  square matrix following the circulant format. As illustrated in Eq (1), the first-row vector (primary vector) in a circulant matrix  $\mathbf{w}_{ij} = [w_{1,ij}, w_{2,ij}, \dots, w_{l,ij}]$  contains all independent parameters, with subsequent rows being circulant reformations of it. Intuitively, compared to general matrices, block-circulant matrices reduce the number of independent parameters to  $MN/l$ .

$$\mathbf{W}_{block} = \left. \begin{array}{c} \overbrace{\begin{bmatrix} \mathbf{W}_{11} & \mathbf{W}_{12} & \dots & \mathbf{W}_{1q} \\ \mathbf{W}_{21} & \mathbf{W}_{22} & \dots & \mathbf{W}_{2q} \\ \vdots & \vdots & \mathbf{W}_{ij} & \vdots \\ \mathbf{W}_{p1} & \mathbf{W}_{p2} & \dots & \mathbf{W}_{pq} \end{bmatrix}}^{N=Q \times l} \end{array} \right\} M=P \times l ; \mathbf{W}_{ij} = \begin{bmatrix} w_{1,ij} & w_{2,ij} & \dots & w_{l,ij} \\ w_{l,ij} & w_{1,ij} & \dots & w_{l-1,ij} \\ \vdots & \vdots & \ddots & \vdots \\ w_{2,ij} & w_{3,ij} & \dots & w_{1,ij} \end{bmatrix} \quad (1)$$

In DNNs, the connection between two layers is typically represented by MVM involving the weight matrix  $\mathbf{W}$  and the input vector  $\mathbf{x}$ , followed by a nonlinear activation function, expressed as  $\mathbf{y} = \sigma(\mathbf{W} \cdot \mathbf{x} + \mathbf{b})$ . Here, vector  $\mathbf{y}$  represents the output vector, and  $\mathbf{b}$  is a bias vector. When  $\mathbf{W}$  is a circulant matrix, the computational complexity of MVM operations can be reduced from  $O(n^2)$  to  $O(n \cdot \log n)$  using the fast Fourier transform (FFT) as:<sup>[19][37]</sup>

$$\mathbf{y} = \mathcal{F}^{-1}(\mathcal{F}(\mathbf{w}) \odot \mathcal{F}(\mathbf{x})) \quad (2)$$

where  $\mathcal{F}(\cdot)$  and  $\mathcal{F}^{-1}(\cdot)$  represent FFT and its inverse (IFFT), respectively;  $\odot$  represents vector element-wise multiplication. This method can also be applied to BCM by partitioning the vector  $\mathbf{x}$  into  $p$  segments and aligning them with the corresponding block  $\mathbf{W}_{ij}$ .

In this work, the ONN imposes structured constraints on the weight matrices of both convolutional and fully-connected (FC) layers, requiring adherence to a block-circulant configuration. It is essential to recognize that while the StrC-ONN share a similar connection topology with traditional DNNs, there is no direct correspondence or conversion between the two architectures. Therefore, the structured constraints need to be embedded during the training stage. Owing to this characteristic, the StrC-ONN could improve efficiency across multiple dimensions. Firstly, the compression strategy significantly reduces the number of model parameters. From a hardware perspective, it decreases the number of active E-O modulators required for weight programming and the control complexity for on-chip inference. Additionally, this strategy conserves memory for weight storage and reduces data access requirements on hardware resources, such as digital-to-analog converters (DACs) and their driver circuits. However, these advantages come with restricted parameter space, presenting a potential trade-off. For instance, a small block size in the BCM yields a lower compression ratio, while a larger size offers substantial compression but may result in accuracy degradation. Related research has demonstrated the mathematical rigor of this approach.<sup>[39]</sup> Specifically, structured networks preserve the universal representability of DNNs, allowing them to approximate or represent functions with complexity comparable to those handled by uncompressed networks. Additionally, with appropriate compression, structured networks maintain comparable performance and accuracies across a wide range of tasks, which has been demonstrated in electrical digital computing.<sup>[19]</sup> In this work, we implemented the compression technique through a compact PIC design that achieves high hardware and power efficiency, and its performance is demonstrated experimentally.

### Operation Mechanism of CirPTC

The operation mechanism of CirPTC and the ONN training framework are shown in Fig. 1. The primary vector  $\mathbf{w}$  is encoded into incoherent light intensity using serial MRRs operating at different wavelengths, which then physically multiply with the input vector  $\mathbf{x}$  encoded by Mach-Zehnder modulators (MZMs). The CirPTC is characterized by a crossbar switch array in which the switches operate at different wavelengths following a circulant arrangement (Fig. 1.b). The switch array maps the elements of a weighted vector to the outputs, thereby directly implementing the structured configuration by the circuit topology. By leveraging the wavelength division multiplexing (WDM), on-chip photodetectors (PDs) can autonomously sum weighted elements at the output ports. Compared to ONN architectures designed for GEMMs, the CirPTC requires only  $M \times N / l$  active MRRs to implement a  $M \times N$  BCM, while the optical switches in the crossbar array are “static” or even passive.<sup>[24]</sup> From a hardware perspective, this configuration significantly reduces reprogramming complexity and the number of DACs required for weight encoding.

As mentioned, the compression mechanism requires partitioning 2-D matrices and embedding

structured constraints. The operation for the FC layers is straightforward because the connection between the two layers can be directly represented by a weight matrix. In convolutional layers, learnable kernels slide over the input data, generating feature maps through convolution operations. Unlike FC layers, convolution operations share kernels and focus on local areas, resulting in inherently sparse connections. To perform convolution operations efficiently, we utilize the “*im2col*” approach, which tiles all kernels and inputs into large 2-D matrices, transforming tensor-based convolution operations into matrix-matrix multiplications.<sup>[40][41]</sup> As illustrated in Fig. 1.a, each kernel comprises of  $C_{in}$  channels with a dimension of  $k \times k \times C_{in}$ , and each set of kernels corresponds to an output feature map. For a convolution layer that includes  $C_{out}$  output features, the kernels can be reorganized into a 2-D weight matrix  $\mathbf{W}$  of size  $C_{out} \times (k \times k \times C_{in})$  by flattening kernels into a 1-D vector and stacking them row-wise. Here, we constrain  $\mathbf{W}$  to a block-circulant format starting from the training stage, and the primary vector  $\mathbf{w}_{ij}$  for each circulant block are encoded by  $N/l$  rails of serial MRRs. Similarly, as the kernel slides across the input image with  $w \times h$  pixels, the corresponding pixels are rearranged into a column vector of dimension  $(k \times k \times C_{in})$  and then stacked to create the input matrix  $\mathbf{X}$ . To perform MVMs with the circulant block, the column vectors in  $\mathbf{X}$  are partitioned into length- $l$  subgroups. Based on this approach, the convolution operation for one feature map translates into  $(w - k + 1) \cdot (h - k + 1)$  MVMs between a BCM and the input vectors of length  $k^2 \times C_{in}$ .

### Training Framework for CirPTC-Based ONN

As an analog computing platform, CirPTC inherently exhibits various hardware-induced nonidealities, including truncated resolution, crosstalk, and fabrication variances. Direct deployment of ML models faces challenges in accurately capturing complex chip behaviors, potentially leading to significant performance degradation. To address these issues, implementing DNNs on CirPTC with enhanced robustness requires a hardware-aware training strategy based on actual measurements. However, training models directly using on-chip optical responses presents an additional challenge, as the data behaves like a lookup table (LUT), which is inherently non-differentiable. In this work, we employ a hardware-aware training framework that incorporates a differentiable PIC estimator (DPE). The general procedures of the training framework are summarized in Fig. 1.d, with additional details provided in Methods. Following quantization and dynamic noise injection, the DPE—featuring two operational modes, differentiable and lookup—enables gradient backpropagation while accounting for chip behaviors. Experimental results demonstrate that this approach effectively compensates for on-chip nonidealities, resulting in improved inference accuracy compared to previous ONN training protocols, such as simulation-based gradient approximation,<sup>[22][42]</sup> and derivative-free optimization.<sup>[43][44]</sup>

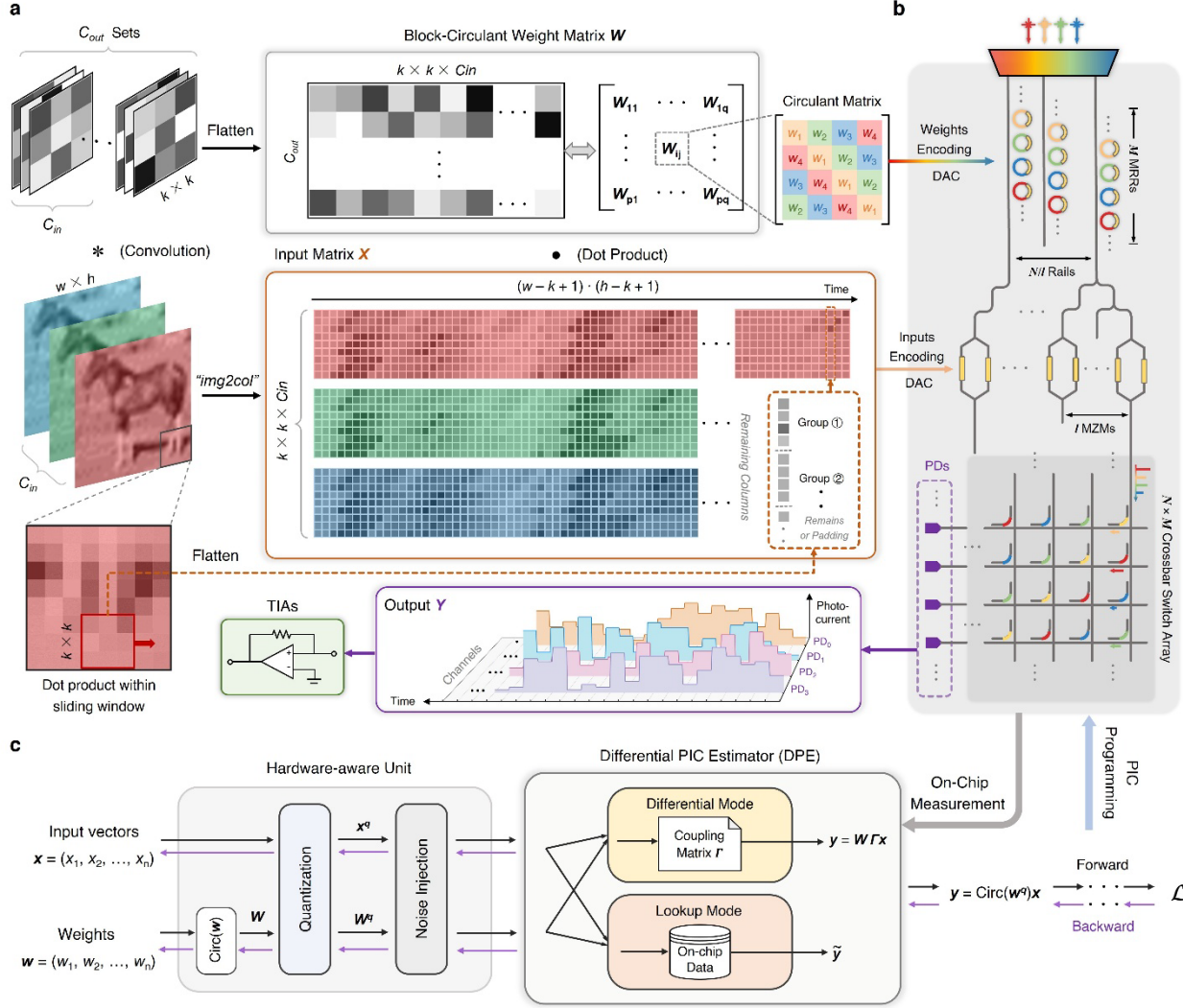


**Fig. 1** General architecture of StrC-ONN and image convolution operations using CirPTC. **a**. Transformation of convolution operations into MVMs and the implementation of BCM on CirPTC. This conceptual illustration shows an input image with 3 channels perform convolution with  $C_{out}$  sets of  $k \times k \times C_{in}$  kernels (where  $k = 3$ ). The 2-D flattened weight matrix  $W$  is configured as a BCM with  $4 \times 4$  circulant blocks. Pixels within the sliding window are partitioned into subgroups of length 4 after flattening and are then sent to the CirPTC. **b**. General schematic of order- $l$  CirPTC with an  $N \times M$  crossbar array. The output photocurrent is detected by oscilloscope or ADC after amplification by the off-chip trans-impedance amplifier (TIA). Here, different colors denote devices operating at different wavelengths **c**. The hardware-aware training framework for CirPTC-based ONN.

## Result

### Design of CirPTC

In this study, we designed and fabricated an order-4 CirPTC. The micrograph of the chip after packaging is shown in Fig. 2.a, with the zoom-in figures of its key components (Fig. 2.b). A

continuous-wave (CW) multiwavelength input is coupled to the chip via an edge coupler. To prevent crosstalk, the operational ranges of 4 MRRs are set to be separated without overlapping in the spectrum, as illustrated in Fig. 2.d. To enable hardware-efficient scalar multiplication  $x^* \cdot w_{ij}$  ( $x^*$  is one element in  $x_j$ ) within a single device, the modulator for input encoding needs to modulate signals across multiple wavelengths simultaneously (Fig. 2.e). This requires modulators with broadband transmission characteristics, like those provided by MZMs based on the phase-tuning mechanism.<sup>[25][45]</sup> For the crossbar switch array, we employed 16 add-drop MRRs, each interconnected with others through shared input and drop bus waveguides along the same row and column. Each MRR is calibrated to a designated wavelength according to the circulant configuration, thereby redirecting the appropriate element from  $x^* \cdot w_{ij}$  to the PDs. Finally, the PDs automatically sum the signals on the column bus waveguide as photocurrent, thereby completing the MVM operation. To avoid distortion of the circulant block, each MRR needs to be calibrated to achieve a uniform maximum output (grey dotted line in Fig. 2.f). The primary advantage of the crossbar array is the small footprint of MRR and the inherent sharing of waveguides, both of which enhance the compactness and scalability. Since these MRRs function exclusively as wavelength-dependent switches, their operating statuses are fixed after calibration. Additionally, cascading each building block enables a one-shot calibration mechanism that minimizes the impact of dynamic nonidealities, such as thermal crosstalk and loss, while simplifying control complexity. Therefore, CirPTC proposes an efficient, customized PIC design through a hardware-software co-design approach, rather than merely exploring algorithmic characteristics in isolation. Further details about system calibration are provided in Supplementary Note 1.

For yield and cost considerations, the CirPTC utilizes thermo-optic modulators from the foundry's Process Design Kit (PDK), with each device type having identical specifications. The ohmic microheaters of MZMs and MRRs are programmed by a multi-channel DAC. Since all MRRs are identical (exhibiting similar resonant wavelengths at zero bias), the four operating wavelengths selected—1545.5, 1551.0, 1560.5, and 1563.0 nm—are spaced separately within a single free spectral range (FSR) to minimize spectral crosstalk (Fig. 2.d&f). In future optimizations, the radius of MRRs can be customized to achieve configurations with different resonant wavelengths, thereby further decreasing power consumption. The on-chip photodetectors, along with off-chip TIAs, convert the optical output to electrical voltage signals, which are then measured by oscilloscopes. The CirPTC is mounted on a customized printed circuit board (PCB) and connected to the control units via wire bonding (Fig. 2.c). To facilitate calibration and monitoring, four monitor ports at the ends of horizontal bus waveguides are coupled to the fiber array. Due to the cascading and independence of the building blocks, we can measure the transmission characteristic of each device through the on-chip photodetector or the monitor port. Based on



measurements and physical models of devices, we fitted the transmission curves of MZMs and MRRs for subsequent demonstrations and experiments (Fig. 2d-f).

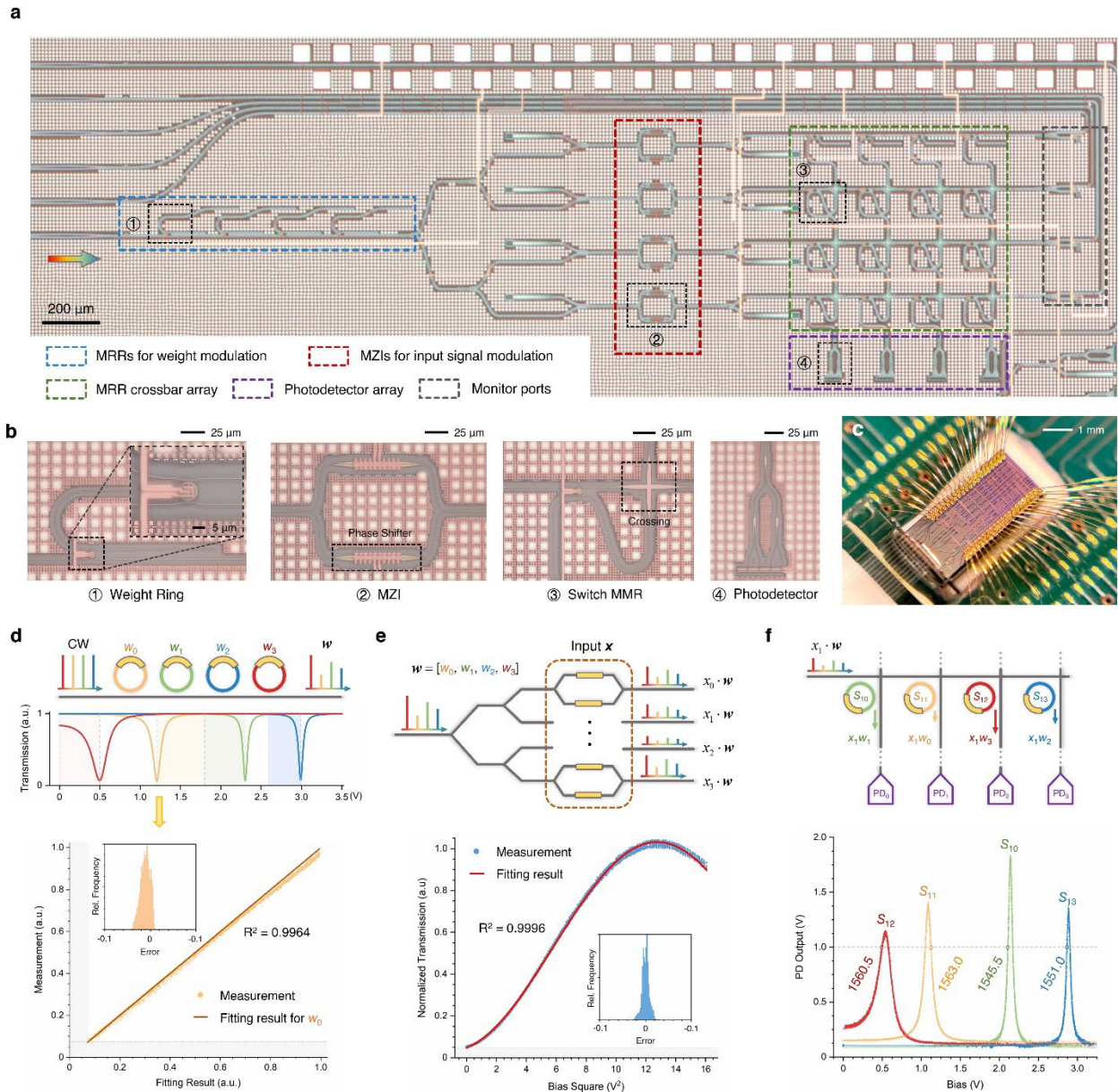


**Fig. 2 Schematic of an order-4 CirPTC.** **a.** Optical micrograph of the CirPTC, featuring five main building blocks. **b.** Key optical components highlighted in a zoomed-in micrograph. **c.** Electrical and optical package for the CirPTC. **d-f.** Illustrations of the operational mechanisms and data flow within each building block of CirPTC. Notably, to avoid spectral overlap, the modulation range for MRRs operating at 1563.0 nm is allocated to the right half-branch of resonate peak, whereas the modulation ranges for the other MRRs are situated on the left branch. The on-chip measurement results (dots in the background) and the fitting results based on physical models are shown in the lower part of figures. Due to the dark current of the photodetector and the asymmetric, lossy coupling of the MRRs,<sup>[46]</sup> a fixed “forbidden zone” (grey area) is established at each output port. However, this can be eliminated through post-processing in the electrical domain. The transmission characteristics of other devices are provided in Supplementary Note 1.

## On-chip image processing

To experimentally illustrate the aforementioned principle, we perform on-chip image processing using convolutional kernels to extract physical features from input images. For demonstration, we selected and implemented several kernels with intuitive physical interpretations. Although CirPTC imposes structured restrictions on the weight matrix, we can still implement arbitrary kernels by exclusively targeting one column in the crossbar array after block-circulant extension (refer to Supplementary Note 5 for details). Firstly, we demonstrate the convolution operation on input images from the CIFAR-10 dataset using a  $3 \times 3$  blur kernel (Fig. 3.a), which results in a  $12 \times 4$  BCM with an addition of 3 rows of padding. Given that the three channels (RGB) are convolved with the same 2D blur kernel, they can be reorganized into an input matrix of  $k^2 \times 3 \cdot (n-k+1)^2$ , where  $k = 3$  and  $n = 32$ . Then, the input matrix  $\mathbf{X}$  encoded by an FPGA with a 4-bit resolution and a time interval of  $\tau = 80 \mu\text{s}$ , corresponding to a data rate of 12.5 Kbaud (Fig. 3.b). Given the extensive weight sharing in CNNs, the bottleneck of data rate primarily arises from the limited output settling time of the DAC ( $20 \mu\text{s}$ ) and the input encoding bandwidth in the tens of KHz range. In future optimizations, the throughput of CirPTC can be increased to GHz levels by utilizing high-speed DACs and E-O modulators, such as carrier-depletion and carrier-accumulation MZMs.<sup>[25][47]</sup> Fig. 3.a presents the on-chip convolution results of four images (see Supplementary Note 5 for results of all images), and Fig. 3.c displays the experimental waveform alongside the expected values (grey lines) for the “horse”. Each time slot in the waveform results from the post-processing summation of the dot products of length-4 subvectors from three groups. The feature maps extracted exhibit a normalized average root mean square error (RMSE) of 0.0243 (Fig. 3.d). Additionally, the deviation between the testing and ideal results typically follows a normal distribution. The deviation is primarily attributed to internal coherent interference in the crossbar array, associated with unexpected leakage from MRRs and spectral crosstalk (further details are discussed in Supplementary Note 6).<sup>[48]</sup>

Since the modulators in the CirPTC operate with an amplitude-tuning mechanism, both the weights and inputs are theoretically required to be positive. For ONNs, employing activation functions such as ReLU, sigmoid, or softmax could ensure that the inputs of each layer remain non-negative. The full-range weights can be achieved by two methods. The first method normalizes  $\mathbf{W}$  to positive values by adding a bias and sets the intermediate values of the dynamic ranges as “0”, thereby generating a reference matrix. The normalized kernels and the reference matrix are implemented independently, with their outputs subsequently subtracted during post-processing. Alternatively,  $\mathbf{W}$  could be split into two matrices based on the sign of its elements, with each matrix being processed on CirPTC separately. One advantage of post-processing subtraction is that it can automatically eliminate the influence of dark current on the output range. Similarly, both methods

can be implemented through spatial or time-domain multiplexing. The spatial approach requires doubling the hardware resources with balanced photodetectors,<sup>[49][50]</sup> while the time-domain multiplexing doubles the processing time and performs subtraction in the digital processor.

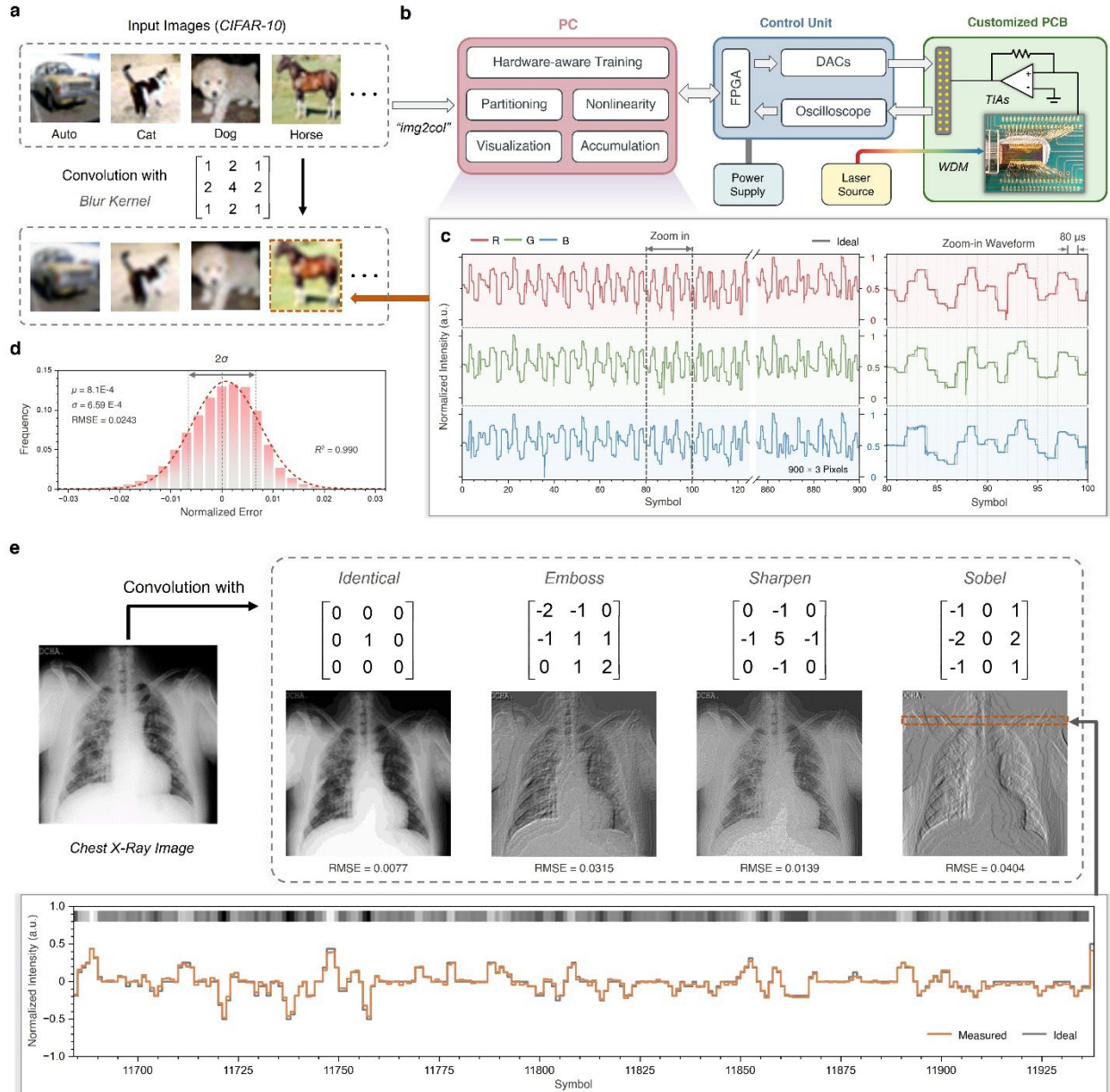


**Fig. 3 Experimental results of the image processing on CirPTC. a.** Input images from CIFAR-10 dataset processed with a  $3 \times 3$  blur kernel. **b.** Schematic of the experimental setup and test flow. Kernels are first block-circulant extended on a PC (for arbitrary kernels) and partitioned into multiple  $4 \times 4$  blocks. Each block and input vectors are then sent to CirPTC in sequential waveforms, controlled by the FPGA and a multi-channel DAC **c.** Ideal and experimental output waveforms for the RGB channels of “horse”, and the sampling rate of oscilloscope is 500KHz (40 data points per symbol). **d.** Statistical analysis of the error between experimental and ideal feature maps for the CIFAR-10 dataset. **e.** X-ray image and the feature maps extracted by four different kernels. Due to the large volume of data, the sampling rate is reduced to 12.5 KHz.

To further evaluate the capability of CirPTC to process full-range weights, we mapped a chest X-ray (CXR) image ( $256 \times 256$  pixels) from the COVID-QU-Ex dataset with a 4-bit resolution,<sup>[51]</sup> processing with multiple  $3 \times 3$  kernels. Here, we employ the time-domain multiplexing, wherein the convolution kernels are split into positive and negative parts, each consisting of three  $4 \times 4$  circulant matrices. Fig. 3.e shows the extracted features from the CXR image, such as the edges of the human lung highlighted by the vertical Sobel kernel.

### **CirPTC-based ONN for classification**

In this work, we assess the performance of CirPTC on classification tasks over three datasets: a simple CNN is applied to the street view house numbers (SVHN) dataset, while a VGG-style neural network is applied to the CIFAR-10 and COVID-QU-Ex datasets. All convolutional and FC layers are implemented on order-4 CirPTC, while batch normalization (BN), pooling, and nonlinear activation are executed on digital processors. Here, the activation control resolution is set to 4 bits, while the weight precision is configured to 6 bits. The COVID-QU-Ex dataset comprises CXR images from individuals diagnosed with COVID-19, those with non-COVID-19 infections (such as other viral or bacterial pneumonia), and healthy controls. For the three-category classification task, the CirPTC-based ONN, as illustrated in Fig. 4.a, achieves a classification accuracy of 92.6%, with a sensitivity of 96.3% and a specificity of 98.0% for COVID-19 diagnosis. Furthermore, CirPTC-based ONN experimentally achieved overall accuracies of 80.04% and 88.08% on CIFAR-10 and SVHN tasks, respectively (Fig. 4 b-d).

Additionally, we evaluated the model performance under various configurations, comparing digital and optical approaches, as well as GEMM-based and structure-compressed networks. As shown in Fig. 4.e, the CirPTC-based implementation maintains competitive performance, exhibiting only a 1.41% to 3.65% accuracy drop compared to full-precision GEMM-based digital baselines while achieving up to 74.91% savings in model parameters. Moreover, compared to a digital implementation with circulant compression, the proposed hardware-aware training strategy with DPE ensures that the accuracy drop is kept below 1%. Note that the experiments and simulation indicate that crosstalk and noise from the photonic chip tend to accumulate along the forward path of the network, leading to increased deviation and potentially significant performance degradation. The DPE can mitigate this issue, particularly in ONNs with deep architectures. However, more sophisticated modeling and quantification of on-chip behavior may be necessary for modern large models.

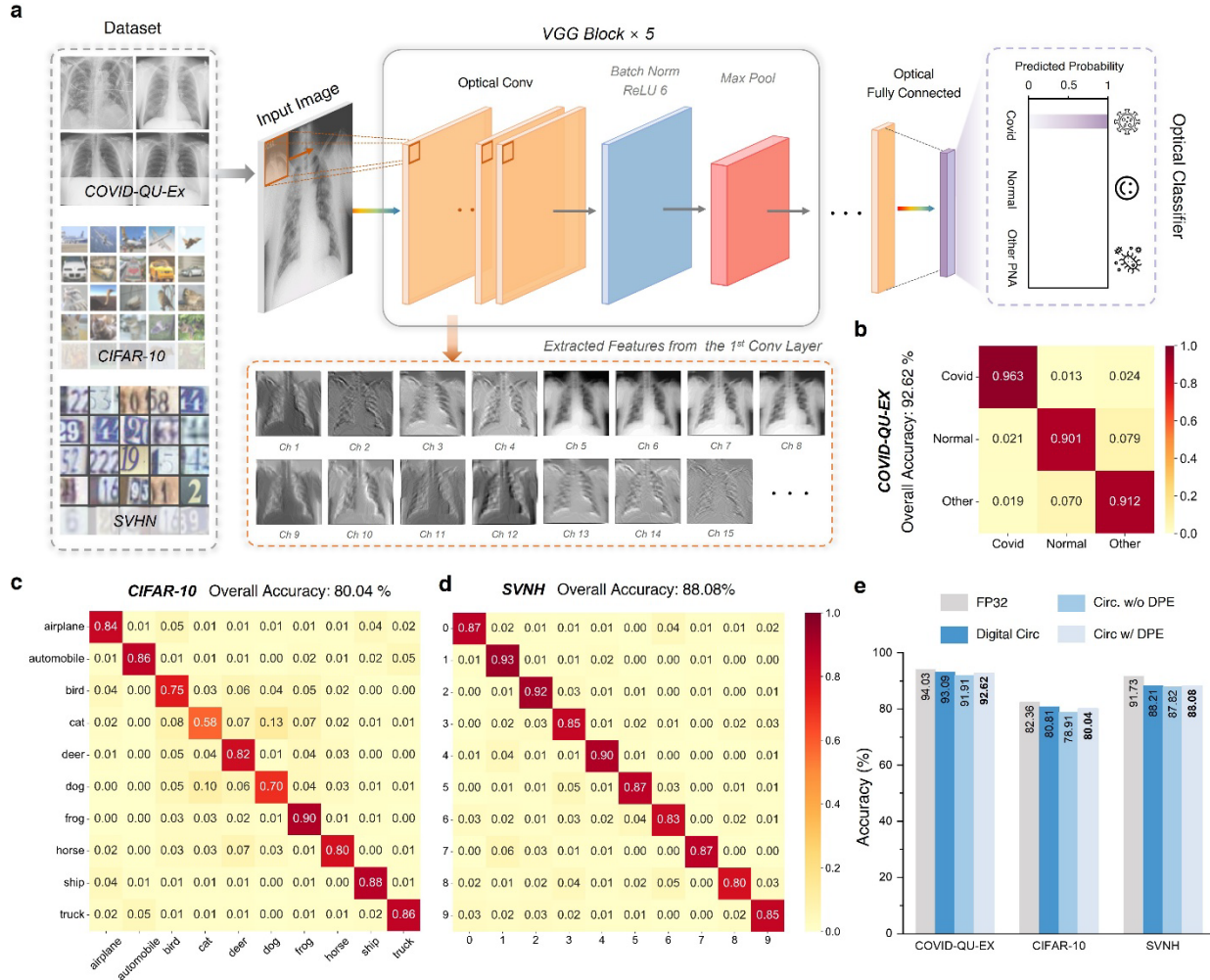


**Fig. 4 Experimental results of the CirPTC-based ONN for image classification.** **a.** Structure of StrC-ONNs with input images from multiple datasets, illustrated with a schematic diagram representing a three-category classification task for the COVID-QU-EX dataset. Detailed descriptions of StrC-ONNs implementation are provided in Supplementary Note 7. **b.-d.** Confusion matrices for the three datasets evaluated. **e.** Comparison of experimental classification accuracies, with and without DPE-based hardware-aware training, against the simulated accuracies of a digitally structured DNN and a GEMM-based DNN using 32-bit floating-point precision.

## Discussion

### Benchmark analysis

This section evaluates the expected performance of our proposed architecture through numerical analysis, including benchmarks such as chip area, insertion loss, computing speed, power consumption, and scalability. The details of the analysis are discussed in the Supplementary Note 8. Unlike the Von Neumann architecture, PTCs can execute an MVM operation within a single clock cycle. Defining an operation as either the multiplication or addition, the throughput of an  $N$

$\times M$  CirPTC can be evaluated by the number of operations per second (OPS), which is quantified as:

$$\text{OPS} = 2MN \cdot f_{op} \quad (3)$$

where  $f_{op}$  represents the operational rate. Clearly, enhancing the throughput can be achieved by implementing a larger matrix and increasing  $f_{op}$ . However, engineering limitations and trade-offs among benchmarks must be considered during the design process. First,  $f_{op}$  is dependent on the on-chip devices and the E-O/O-E conversion process. The CirPTC prototype based on thermo-optic devices that we demonstrated experimentally exhibits a tuning speed of tens of KHz.<sup>[52]</sup> To fully harness the potential of optical computing, operands must be programmed at high speed. To achieve high-speed operation, free-carrier-effect-based MZMs operating in carrier-depletion (reverse-bias  $p$ - $n$  junction) or carrier-accumulation/metal-oxide-semiconductor capacitor (MOSCAP) modes can replace the thermo-optic MZMs for input encoding in this proof-of-concept demonstration.<sup>[25][53][54]</sup> Unlike the dynamic input  $\mathbf{x}$ , which updates with each clock cycle, the weights can be shared and remain constant during the inference phase. Therefore, we assume that the modulation speed of thermo-tuned MRRs is sufficient to support the time-domain hardware reuse required for DNNs. Additionally, another factor restricting  $f_{op}$  is the delay in PICs. To implement an MVM operation within a single clock cycle, the system clock period  $1/f_{op}$  should be no less than the total latency of the CirPTC, which increases linearly with the matrix size. Alternatively, clock synchronization techniques could enable higher  $f_{op}$  while preventing sampling errors.<sup>[55]</sup>

The computing density, defined by the OPS divided by the chip area, is 4.85 TOPS/mm<sup>2</sup> for a 48  $\times$  48 CirPTC operating at 10 GHz. Note that modulators based on the carrier effect typically require larger footprints than thermo-optic devices due to their lower tuning efficiencies and the potential requirement for traveling-wave electrodes to achieve high-speed modulation.

The total power consumption of CirPTC comprises the power to drive lasers, load operands ( $\mathbf{X}$  and  $\mathbf{W}$ ), detect signals, and the static power required to maintain PIC in the operating state. For CirPTC, the static power consumption primarily arises from calibrating MRRs to the desired operating wavelength and maintaining the resonated state, which is negligible when using customized MRRs or post-fabrication nonvolatile phase trimming techniques to correct fabrication variations.<sup>[56]</sup> Additionally, depletion-mode/MOSCAP or nonvolatile devices can potentially eliminate static power consumption.<sup>[24]</sup> Based on the references and the experimental results,<sup>[52][54]</sup> we estimate that each MOSCAP MZM consumes 0.35 pJ per symbol, with each MRR requiring 3 mW to maintain the weight. For output signal detection, the ADC power consumption is 39 mW at 10 GHz and 194 mW at 25 GHz,<sup>[57]</sup> while the TIA energy consumption is 0.65 pJ/bit.<sup>[58]</sup> Despite the availability of high-speed receivers, the high power consumption of the ADC could be the

dominant factor, reducing overall power efficiency (Figure S16.b & f). The minimum required laser power must overcome the capacitance and shot noise of the photodetector, as well as to compensate for the insertion loss encountered along the critical path of the PIC.<sup>[59]</sup> Notably, the insertion loss of CirPTC in the critical path increases linearly with matrix size (Figure S14), resulting in an exponential increase in laser power. As shown in Figure S16.e, laser power constitutes 43.14% of the total power when  $M = N = 64$ , and power efficiency begins to decline. According to our calculations, a  $48 \times 48$  CirPTC configuration achieves the peak power efficiencies of 9.53 TOPS/W. This achieves  $3.82\times$  power efficiency higher than those of uncompressed MRR-based crossbar arrays. Beyond the on-chip power consumption, the energy required for storing and memory reconfiguration should also be considered. In this work, the memory cost for storing and accessing the weight matrix, as well as the energy required to reconfigure active devices, is reduced by a factor of  $l$  in order- $l$  CirPTC compared to ONN architectures designed for GEMMs.

In addition to the insertion loss, the scalability of CirPTC is also constrained by the limited density of MRR resonant peaks on the spectrum. Specifically, we encode the weights onto different wavelengths and use WDM techniques to perform  $M \times N$  MVM operations across  $N$  WDM channels. To avoid errors stemming from spectral crosstalk, the FSR of MRRs needs to accommodate  $N$  resonant peaks with permissible overlap, which is evaluated in terms of weight resolution. Based on modeling and numerical analysis, the required  $Q$  value for a 6-bit weight resolution is  $2.49 \times 10^5$  when  $N = 48$  (Fig. S5). Although silicon MRRs and microdisk resonators with high  $Q$  values above  $2 \times 10^7$  have been widely reported,<sup>[60]-[62]</sup> fabrication variation and narrow electrical tuning range should be considered.

## Spectral folding

Note that the MRR in the crossbar array functions solely as a wavelength-dependent switch. To further reduce the crossbar array size and enhance CirPTC performance, we propose a spectral folding scaling approach. Specifically, by exploiting its periodicity, a single MRR can redirect signals at different wavelengths across multiple FSRs. This approach enables an  $N \times M$  crossbar array to perform the MVM of a BCM with dimensions  $M \times (r \cdot N)$  and a length- $r \cdot N$  input vector, where  $r$  is the fold number (Figure S18.a). Through spectral folding, the footprint and loss of PIC will be further decreased, thereby improving computing density and power efficiency. Numerical analysis shows that with  $r = 4$  and  $M = N = 48$ , CirPTC achieves a computing density of 5.48 TOPS/mm<sup>2</sup> and a power efficiency of 17.13 TOPS/W ( $6.87\times$  higher than uncompressed MRR-based ONNs), respectively. The significant improvement in power efficiency arises from increased operational throughput without expanding the number of ADCs and TIAs, while the thermal power consumption of the MRRs for weight programming becomes the dominant factor (Figure S18.b). By utilizing depletion-mode/MOSCAP MRRs, this component of power can be potentially

eliminated and the power efficiency can be increased to 47.94 TOPS/W. However, this approach requires more stringent calibration and compensation from the dynamic range of weight programming or laser power due to the wavelength-dependent response of PDs. A detailed comparison with state-of-the-art (SOTA) optical and electrical computing architectures is provided in Table S6.

## Conclusion

In this work, we propose CirPTC, a scalable photonic-electric hybrid AI accelerator with a hardware-efficient ONN architecture using a structured compression technique. We experimentally demonstrate on-chip convolution processing of large-scale images. Then, the StrC-ONN architecture is implemented on the order-4 CirPTC for image classification tasks. By reasonable scaling and spectral folding approach, the proposed design achieves  $6.87\times$  higher power efficiency compared to uncompressed MRR-based ONNs, while using  $\sim 25\%$ - $35\%$  of model parameters, active optical components, and memory usage. Additionally, we employ a hardware-aware training framework incorporating the DPE, which efficiently models the on-chip behavior of CirPTC, accounting for nonidealities such as inherent crosstalk and noise, thereby boosting the model robustness. Notably, CirPTC-based ONNs with circulant structured compression achieve comparable performance across multiple datasets to full-precision digital GEMM-based DNNs, demonstrating negligible loss in accuracy. Furthermore, the compression strategy and the DPE-based training framework can be extended to existing PICs, enhancing their hardware and power efficiency. These findings offer a novel route to overcoming the bottlenecks of optical computing, thus paving the way for next-generation high-performance AI accelerators in the post-Moore era.

## Methods

### Testing setup

Except for the CirPTC chip, manufactured by *AIM Photonics*, all other devices and instruments used for testing are commercially available components. The PIC layout was developed and verified in *Synopsys Optodesigner*. The control signals are routed to the pads located at edges, which are then wire-bonded to a customized PCB. We configure the control signals using a 40-channel, 14-bit DAC (AD5370, Analog Devices), controlled by an FPGA (PYNQ-Z2) via the serial peripheral interface (SPI) protocol, followed by analog signal buffers (TLE2064, Texas Instruments). The system power supply, which includes  $\pm 12\text{V}$  for the analog circuit and a 1V bias for the photodetector, is provided by a triple-output DC power supply (E3630A, Agilent). The optical inputs are generated by tunable CW laser sources (CoBrite DX4, ID Photonics), and the polarization of the light beams is then tuned by polarization controllers (OZ Optics). An 8-channel



single-mode fiber array (Meisu Technology Co., Ltd.) is used to couple the input into CirPTC via edge couplers. The transmission spectra are measured using broadband amplified spontaneous emission sources (ASE-FL7001P, ThorLabs) and optical spectrum analyzers (AQ6317B, Ando). The output photocurrents are amplified by the TIAs (LT1216CN, Analog Devices) and detected using two oscilloscopes (Analog Discovery 2, Digilent). The entire system is controlled by an FPGA, with data acquisition performed via the application programming interface (API) for oscilloscopes.

## Hardware-Aware Training

The proposed training framework for CirPTC-based ONN operates in two modes:

- *Lookup Mode* is used for inference, leveraging actual measurement data corresponding to specific inputs and weights.
- *Differentiable Mode*, which mimics actual on-chip behaviors, ensures that the model is trained with awareness of noise and nonidealities while maintaining differentiability for backpropagation.

For each layer, whether linear or convolutional, we represent it as an MVM operation. Here, large MVMs are partitioned into small matrices, each implemented on the CirPTC using a specific weight block  $W$  and the corresponding input vector  $\mathbf{x}$ .  $W$  and  $\mathbf{x}$  are quantized 4-bit and 6-bit precision, denoted as  $W^q$  and  $\mathbf{x}^q$ , respectively, before being mapped for actual testing during inference:

$$\begin{aligned} W^q &= Q(W), \quad \mathbf{x}^q = Q(\mathbf{x}) \\ \mathbf{y} &= f(W^q \cdot \mathbf{x}^q) = \text{Circ}(\mathbf{w}^q) \cdot \mathbf{x} \end{aligned} \quad (4)$$

where each primary vector  $\mathbf{w}$  is expanded into a circulant representation, and  $f(\mathbf{w}, \mathbf{x})$  represents the LUT derived from on-chip measurement. Since  $f(\mathbf{w}, \mathbf{x})$  is non-differentiable, we approximate its behavior by modeling the response of the actual physical chip. Our analysis identifies crosstalk—caused by unexpected coherent interference within the crossbar array (see Supplementary Note 6 for details)—as the primary noise source. Furthermore, the cascaded PIC topology ensures that the weight encoding within the CirPTC is effectively isolated from other components, resulting in a negligible impact on the crossbar array. By sweeping through all possible input combinations, we obtain the LUT of on-chip response  $Y(\mathbf{x})$ , and  $\Gamma$  is then determined by minimizing the following objective:

$$\Gamma = \operatorname{argmin}_{\Gamma, Y(\mathbf{x})} |Y(\mathbf{x}) - \Gamma \mathbf{x}| \quad (5)$$

Using the AI-assisted approach, we can approximate the forward-pass computation as  $Y'(\mathbf{w}, \mathbf{x}) = W \cdot \Gamma \mathbf{x}$ , which enables gradient propagation with respect to both  $\mathbf{w}$  and  $\mathbf{x}$ .

## Competing interests

The authors declare no competing financial or associative interests that could be construed as a conflict of interest with respect to the research reported in this paper.

## Acknowledgements

The authors acknowledge support provided by the Multidisciplinary University Research Initiative (MURI) program under contract No. FA9550-17-1-0071 and the Air Force Office of Scientific Research (AFOSR) under contract No. FA9550-23-1-0452.

## Reference

- [1] LeCun, Yann, Yoshua Bengio, and Geoffrey Hinton. "Deep learning." *nature* 521, no. 7553 (2015): 436-444.
- [2] He, Kaiming, Xiangyu Zhang, Shaoqing Ren, and Jian Sun. "Deep residual learning for image recognition." In *Proceedings of the IEEE conference on computer vision and pattern recognition*, pp. 770-778. 2016.
- [3] Redmon, Joseph, Santosh Divvala, Ross Girshick, and Ali Farhadi. "You only look once: Unified, real-time object detection." In *Proceedings of the IEEE conference on computer vision and pattern recognition*, pp. 779-788. 2016.
- [4] Krizhevsky, Alex, Ilya Sutskever, and Geoffrey E. Hinton. "Imagenet classification with deep convolutional neural networks." *Advances in neural information processing systems* 25 (2012).
- [5] Bojarski, Mariusz, Davide Del Testa, Daniel Dworakowski, Bernhard Firner, Beat Flepp, Prasoon Goyal, Lawrence D. Jackel, et al. 2016. "End to End Learning for Self-Driving Cars." *arXiv preprint arXiv:1604.07316*.
- [6] Sutskever, Ilya, Oriol Vinyals and Quoc V. Le. "Sequence to Sequence Learning with Neural Networks." *ArXiv abs/1409.3215* (2014): n. pag.
- [7] Devlin, Jacob, Ming-Wei Chang, Kenton Lee, and Kristina Toutanova. 2019. "BERT: Pre-training of Deep Bidirectional Transformers for Language Understanding." *arXiv preprint arXiv:1810.04805*.
- [8] Hannun, Awni Y., Pranav Rajpurkar, Masoumeh Haghpanahi, Geoffrey H. Tison, Codie Bourn, Mintu P. Turakhia, and Andrew Y. Ng. "Cardiologist-level arrhythmia detection and classification in ambulatory electrocardiograms using a deep neural network." *Nature medicine* 25, no. 1 (2019): 65-69.
- [9] Cao, Kai, Yingda Xia, Jiawen Yao, Xu Han, Lukas Lambert, Tingting Zhang, Wei Tang et al. "Large-scale pancreatic cancer detection via non-contrast CT and deep learning." *Nature medicine* 29, no. 12 (2023): 3033-3043.
- [10] Lewis, M. "Bart: Denoising sequence-to-sequence pre-training for natural language generation, translation, and comprehension." *arXiv preprint arXiv:1910.13461* (2019).
- [11] Brown, Tom B., Benjamin Mann, Nick Ryder, Melanie Subbiah, Jared Kaplan, Prafulla Dhariwal, Arvind Neelakantan, et al. 2020. "Language Models are Few-Shot Learners." *arXiv preprint arXiv:2005.14165*.
- [12] Yang, Jingfeng, Hongye Jin, Ruixiang Tang, Xiaotian Han, Qizhang Feng, Haoming Jiang, Shaochen Zhong, Bing Yin, and Xia Hu. "Harnessing the power of llms in practice: A survey on chatgpt and beyond." *ACM Transactions on Knowledge Discovery from Data* 18, no. 6 (2024): 1-32.
- [13] Zhang, Chen, Peng Li, Guangyu Sun, Yijin Guan, Bingjun Xiao, and Jason Cong. "Optimizing FPGA-based accelerator design for deep convolutional neural networks." In *Proceedings of the 2015 ACM/SIGDA international symposium*

- on field-programmable gate arrays, pp. 161-170. 2015.
- [14] Li, Huimin, Xitian Fan, Li Jiao, Wei Cao, Xuegong Zhou, and Lingli Wang. "A high performance FPGA-based accelerator for large-scale convolutional neural networks." In *2016 26th International Conference on Field Programmable Logic and Applications (FPL)*, pp. 1-9. IEEE, 2016.
- [15] Jouppi, Norman P., Cliff Young, Nishant Patil, David Patterson, Gaurav Agrawal, Raminder Bajwa, Sarah Bates et al. "In-datacenter performance analysis of a tensor processing unit." In *Proceedings of the 44th annual international symposium on computer architecture*, pp. 1-12. 2017.
- [16] Waldrop, M. Mitchell. "More than moore." *Nature* 530, no. 7589 (2016): 144-148.
- [17] Fang, Fengzhou, Nan Zhang, Dongming Guo, Kornel Ehmann, Benny Cheung, Kui Liu, and Kazuya Yamamura. "Towards atomic and close-to-atomic scale manufacturing." *International Journal of Extreme Manufacturing* 1, no. 1 (2019): 012001.
- [18] Reed, Daniel, Dennis Gannon, and Jack Dongarra. "Reinventing high performance computing: challenges and opportunities." *arXiv preprint arXiv:2203.02544* (2022).
- [19] Ding, Caiwen, Siyu Liao, Yanzhi Wang, Zhe Li, Ning Liu, Youwei Zhuo, Chao Wang et al. "Circnn: accelerating and compressing deep neural networks using block-circulant weight matrices." In *Proceedings of the 50th Annual IEEE/ACM International Symposium on Microarchitecture*, pp. 395-408. 2017.
- [20] Ambrogio, Stefano, Pritish Narayanan, Hsin-yu Tsai, Robert M. Shelby, Irem Boybat, Carmelo Di Nolfo, Severin Sidler et al. "Equivalent-accuracy accelerated neural-network training using analogue memory." *Nature* 558, no. 7708 (2018): 60-67.
- [21] Li, Can, Miao Hu, Yunning Li, Hao Jiang, Ning Ge, Eric Montgomery, Jiaming Zhang et al. "Analogue signal and image processing with large memristor crossbars." *Nature electronics* 1, no. 1 (2018): 52-59.
- [22] Shen, Yichen, Nicholas C. Harris, Scott Skirlo, Mihika Prabhu, Tom Baehr-Jones, Michael Hochberg, Xin Sun et al. "Deep learning with coherent nanophotonic circuits." *Nature photonics* 11, no. 7 (2017): 441-446
- [23] Tait, Alexander N., Thomas Ferreira De Lima, Ellen Zhou, Allie X. Wu, Mitchell A. Nahmias, Bhavin J. Shastri, and Paul R. Prucnal. "Neuromorphic photonic networks using silicon photonic weight banks." *Scientific reports* 7, no. 1 (2017): 7430.
- [24] Feldmann, Johannes, Nathan Youngblood, Maxim Karpov, Helge Gehring, Xuan Li, Maik Stappers, Manuel Le Gallo et al. "Parallel convolutional processing using an integrated photonic tensor core." *Nature* 589, no. 7840 (2021): 52-58.
- [25] Ning, Shupeng, Hanqing Zhu, Chenghao Feng, Jiaqi Gu, Zhixing Jiang, Zhoufeng Ying, Jason Midkiff et al. "Photonic-Electronic Integrated Circuits for High-Performance Computing and AI Accelerators." *Journal of Lightwave Technology* (2024).
- [26] Xu, Xingyuan, Mengxi Tan, Bill Corcoran, Jiayang Wu, Andreas Boes, Thach G. Nguyen, Sai T. Chu et al. "11 TOPS photonic convolutional accelerator for optical neural networks." *Nature* 589, no. 7840 (2021): 44-51.
- [27] Xu, Zhihao, Tiankuang Zhou, Muzhou Ma, ChenChen Deng, Qionghai Dai, and Lu Fang. "Large-scale photonic chiplet Taichi empowers 160-TOPS/W artificial general intelligence." *Science* 384, no. 6692 (2024): 202-209.
- [28] Feldmann, Johannes, Nathan Youngblood, C. David Wright, Harish Bhaskaran, and Wolfram HP Pernice. "All-optical spiking neurosynaptic networks with self-learning capabilities." *Nature* 569, no. 7755 (2019): 208-214.
- [29] Gan, Ji, Weiqiang Wang, and Ke Lu. "Compressing the CNN architecture for in-air handwritten Chinese character recognition." *Pattern Recognition Letters* 129 (2020): 190-197.
- [30] Han, Song, Huizi Mao, and William J. Dally. "Deep compression: Compressing deep neural networks with pruning,

- trained quantization and huffman coding." *arXiv preprint arXiv:1510.00149* (2015).
- [31] Molchanov, Pavlo, Stephen Tyree, Tero Karras, Timo Aila, and Jan Kautz. "Pruning convolutional neural networks for resource efficient inference." *arXiv preprint arXiv:1611.06440* (2016).
- [32] Jaderberg, Max, Andrea Vedaldi, and Andrew Zisserman. "Speeding up convolutional neural networks with low rank expansions." *arXiv preprint arXiv:1405.3866* (2014).
- [33] Tai, Cheng, Tong Xiao, Yi Zhang, and Xiaogang Wang. "Convolutional neural networks with low-rank regularization." *arXiv preprint arXiv:1511.06067* (2015).
- [34] Li, Zhe, Shuo Wang, Caiwen Ding, Qinru Qiu, Yanzhi Wang, and Yun Liang. "Efficient recurrent neural networks using structured matrices in fpgas." *arXiv preprint arXiv:1803.07661* (2018).
- [35] Gu, Jiaqi, Zheng Zhao, Chenghao Feng, Zhoufeng Ying, Mingjie Liu, Ray T. Chen, and David Z. Pan. "Toward hardware-efficient optical neural networks: Beyond FFT architecture via joint learnability." *IEEE Transactions on Computer-Aided Design of Integrated Circuits and Systems* 40, no. 9 (2020): 1796-1809.
- [36] Feng, Chenghao, Jiaqi Gu, Hanqing Zhu, Zhoufeng Ying, Zheng Zhao, David Z. Pan, and Ray T. Chen. "A compact butterfly-style silicon photonic-electronic neural chip for hardware-efficient deep learning." *Acs Photonics* 9, no. 12 (2022): 3906-3916.
- [37] Mathieu, Michael, Mikael Henaff, and Yann LeCun. "Fast training of convolutional networks through ffts." *arXiv preprint arXiv:1312.5851* (2013).
- [38] Lin, Sheng, Ning Liu, Mahdi Nazemi, Hongjia Li, Caiwen Ding, Yanzhi Wang, and Massoud Pedram. "FFT-based deep learning deployment in embedded systems." In *2018 Design, Automation & Test in Europe Conference & Exhibition (DATE)*, pp. 1045-1050. IEEE, 2018.
- [39] Zhao, Liang, Siyu Liao, Yanzhi Wang, Zhe Li, Jian Tang, and Bo Yuan. "Theoretical properties for neural networks with weight matrices of low displacement rank." In *international conference on machine learning*, pp. 4082-4090. PMLR, 2017.
- [40] Chellapilla, Kumar, Sidd Puri, and Patrice Simard. "High performance convolutional neural networks for document processing." In *Tenth international workshop on frontiers in handwriting recognition*. Suvisoft, 2006.
- [41] Jia, Yangqing, Evan Shelhamer, Jeff Donahue, Sergey Karayev, Jonathan Long, Ross Girshick, Sergio Guadarrama, and Trevor Darrell. "Caffe: Convolutional architecture for fast feature embedding." In *Proceedings of the 22nd ACM international conference on Multimedia*, pp. 675-678. 2014.
- [42] Zhang, Tian, Jia Wang, Yihang Dan, Yuxiang Lanqiu, Jian Dai, Xu Han, Xiaojuan Sun, and Kun Xu. "Efficient training and design of photonic neural network through neuroevolution." *Optics Express* 27, no. 26 (2019): 37150-37163.
- [43] Wright, Logan G., Tatsuhiro Onodera, Martin M. Stein, Tianyu Wang, Darren T. Schachter, Zoey Hu, and Peter L. McMahon. "Deep physical neural networks trained with backpropagation." *Nature* 601, no. 7894 (2022): 549-555.
- [44] Spall, James, Xianxin Guo, and Alexander I. Lvovsky. "Hybrid training of optical neural networks." *Optica* 9, no. 7 (2022): 803-811.
- [45] Dwivedi, Sarvagya, Alfonso Ruocco, Michael Vanslebrouck, Thijs Spuesens, Peter Bienstman, Pieter Dumon, Thomas Van Vaerenbergh, and Wim Bogaerts. "Experimental extraction of effective refractive index and thermo-optic coefficients of silicon-on-insulator waveguides using interferometers." *Journal of Lightwave Technology* 33, no. 21 (2015): 4471-4477.
- [46] Van, Vien. *Optical microring resonators: theory, techniques, and applications*. CRC Press, 2016.
- [47] Sludds, Alexander, Saumil Bandyopadhyay, Zaijun Chen, Zhizhen Zhong, Jared Cochrane, Liane Bernstein, Darius Bunandar et al. "Delocalized photonic deep learning on the internet's edge." *Science* 378, no. 6617 (2022): 270-

276.

- [48] Ohno, Shuhei, Rui Tang, Kasidit Toprasertpong, Shinichi Takagi, and Mitsuru Takenaka. "Si microring resonator crossbar array for on-chip inference and training of the optical neural network." *Acs Photonics* 9, no. 8 (2022): 2614-2622.
- [49] Youngblood, Nathan, Sadra Rahimi Kari, Nicholas Nobile, Vivswan Shah, and Dominique Pantin. "Realization of an integrated photonic platform for coherent photo-electric processing." (2023).
- [50] Gu, Jiaqi, Chenghao Feng, Zheng Zhao, Zhoufeng Ying, Mingjie Liu, Ray T. Chen, and David Z. Pan. "SqueezeLight: Towards scalable optical neural networks with multi-operand ring resonators." In *2021 Design, Automation & Test in Europe Conference & Exhibition (DATE)*, pp. 238-243. IEEE, 2021.
- [51] Tahir, Anas M., Muhammad E. H. Chowdhury, Yazan Qiblawey, Amith Khandakar, Tawsifur Rahman, Serkan Kiranyaz, Uzair Khurshid, Nabil Ibtehaz, Sakib Mahmud, and Maymouna Ezeddin. 2022. "COVID-QU-Ex Dataset." Kaggle. <https://www.kaggle.com/dsv/3122958>.
- [52] Timurdogan, Erman, Zhan Su, Ren-Jye Shiue, Christopher V. Poulton, Matthew J. Byrd, Simon Xin, and Michael R. Watts. "APSUNY process design kit (PDKv3. 0): O, C and L band silicon photonics component libraries on 300mm wafers." In *Optical Fiber Communication Conference*, pp. Tu2A-1. Optica Publishing Group, 2019.
- [53] Wang, Jing, Chao Qiu, Hao Li, Wei Ling, Le Li, Albert Pang, Zhen Sheng et al. "Optimization and demonstration of a large-bandwidth carrier-depletion silicon optical modulator." *Journal of lightwave technology* 31, no. 24 (2013): 4119-4125.
- [54] Hiraki, Tatsuro, Takuma Aihara, Koichi Hasebe, Koji Takeda, Takuro Fujii, Takaaki Kakitsuka, Tai Tsuchizawa, Hiroshi Fukuda, and Shinji Matsuo. "Heterogeneously integrated iii-v/si mos capacitor mach-zehnder modulator." *Nature Photonics* 11, no. 8 (2017): 482-485.
- [55] Kihara, Masami, Sadayasu Ono, and Pekka Eskelinen. *Digital clocks for synchronization and communications*. Artech House, 2006.
- [56] Jayatileka, Hasitha, Harel Frish, Ranjeet Kumar, John Heck, Chaoxuan Ma, Meer N. Sakib, Duanni Huang, and Haisheng Rong. "Post-fabrication trimming of silicon photonic ring resonators at wafer-scale." *Journal of Lightwave Technology* 39, no. 15 (2021): 5083-5088.
- [57] ADC (Analog-to-Digital converters)–Alphacore. <https://www.alphacoreinc.com/adc-analog-to-digital-converters/> (accessed 2024-10-20)
- [58] Szilagyi, Laszlo, Jan Pliva, Ronny Henker, David Schoeniger, Jarosław P. Turkiewicz, and Frank Ellinger. "A 53-Gbit/s optical receiver frontend with 0.65 pJ/bit in 28-nm bulk-CMOS." *IEEE Journal of Solid-State Circuits* 54, no. 3 (2018): 845-855.
- [59] Nahmias, Mitchell A., Thomas Ferreira De Lima, Alexander N. Tait, Hsuan-Tung Peng, Bhavin J. Shastri, and Paul R. Prucnal. "Photonic multiply-accumulate operations for neural networks." *IEEE Journal of Selected Topics in Quantum Electronics* 26, no. 1 (2019): 1-18.
- [60] Nijem, Jinan, Alex Naiman, Roy Zektzer, Christian Frydendahl, Noa Mazurski, and Uriel Levy. "High-Q and high finesse silicon microring resonator." *Optics Express* 32, no. 5 (2024): 7896-7906.
- [61] Li, Guanyu, Pei Liu, Xiaoshun Jiang, Chao Yang, Jiyang Ma, Hongya Wu, and Min Xiao. "High-Q silica microdisk optical resonators with large wedge angles on a silicon chip." *Photonics Research* 3, no. 5 (2015): 279-282.
- [62] Gu, Jiabin, Jie Liu, Ziqi Bai, Han Wang, Xinyu Cheng, Guanyu Li, Menghua Zhang et al. "Dry-etched ultrahigh-Q silica microdisk resonators on a silicon chip." *Photonics Research* 9, no. 5 (2021): 722-725.